


Supernovae vs. AGN: Clues to the origin of Fermi Bubbles from OVIII/OVII line ratio

Kartick C. Sarkar^{1,2} *, Biman B. Nath¹, Prateek Sharma²

¹*Raman Research Institute, Sadashiva Nagar, Bangalore 560080, India*

²*Joint Astronomy Programme and Department of Physics, Indian Institute of Science, Bangalore 560012, India*

5 October 2016

ABSTRACT

We constrain the origin of Fermi Bubbles using 2D hydrodynamical simulations of both star formation driven and black hole accretion driven wind models. We compare our results with recent observations of OVIII to OVII line ratio within and near Fermi Bubbles. Our results suggest that independent of the driving mechanisms, a low luminosity ($\mathcal{L} \sim 5 - 7 \times 10^{40} \text{ erg s}^{-1}$) energy injection best reproduces the observed line ratio for which the shock temperature is $\approx 3 \times 10^6 \text{ K}$. Assuming the Galactic halo temperature to be $2 \times 10^6 \text{ K}$, we estimate the shock velocity to be $\sim 300 \text{ km s}^{-1}$. The corresponding estimated age of the Fermi bubbles is $\sim 15 - 20 \text{ Myr}$. Such an event can be produced either by a star formation rate of $\sim 0.5 \text{ M}_{\odot} \text{ yr}^{-1}$ at the Galactic centre or a very low luminosity jet/accretion wind arising from the central black hole.

Key words: Galaxy: center – Galaxy: halo – ISM : jets and outflows – galaxies: star formation

1 INTRODUCTION

The discovery of Fermi Bubbles (FBs) (Su et al. 2010; Ackermann et al. 2014) has given a boost for studying the interaction of Galactic wind and the circum-galactic medium (CGM) of the Milky Way (MW). They are also excellent laboratories to study high energy physics phenomena in such systems as they produce radiation ranging from radio to gamma-rays. However, the dynamical and spectral origin of these bubbles still remain debatable even after ~ 6 years of their discovery.

The dynamical models of the FBs can be divided mainly into two categories. First, AGN driven models in which the bubbles originate from a past accretion activity of the MW central black hole over a time scale of 3–12 Myr, with a luminosity of $\sim 2 \times 10^{41} - 10^{43} \text{ erg s}^{-1}$, either via an accretion wind (AGNW) (Mou et al. 2014, 2015) or via a jet (Guo & Mathews 2012; Yang et al. 2012) from the Galactic centre black hole. Second, a star formation (SF) driven wind model (SFW) in which the bubbles originate from supernovae activity due to star formation at the centre of our Galaxy (Lacki 2014; Crocker et al. 2014b; Sarkar et al. 2015b). Based on the star formation rate (SFR) at the centre, the age of the

bubbles has been estimated to range from $\sim 25 \text{ Myr}$ (Sarkar et al. 2015b, hereafter, S15) to $\sim 200 \text{ Myr}$ (Crocker et al. 2014b).

Although the observations suggest that the current accretion rate of the Galactic centre black hole (GCBH) is $\sim 10^{-9} - 10^{-7} \text{ M}_{\odot} \text{ yr}^{-1}$ (Quataert & Gruzinov 2000; Agol 2000; Yuan, Quataert & Narayan 2003; Marrone et al. 2006) corresponding to a mechanical luminosity of $\sim 5 \times 10^{36-38} \text{ erg s}^{-1}$, it has been suggested that it could have been a few orders of magnitude higher in the past (Totani et al. 2006). On the other hand, infra-red observations suggest that the current SFR is $\approx 0.1 \text{ M}_{\odot} \text{ yr}^{-1}$ (Yusuf-Zadeh et al. 2009), compared to the rate of $\approx 0.3 \text{ M}_{\odot} \text{ yr}^{-1}$ required to produce the bubbles (Sarkar et al. 2015b). Interestingly, a recent observation by Molinari et al. (2012) has revealed a molecular ring of size $\sim 100 \text{ pc}$ at the Galactic centre which can potentially harbour a higher rate of star formation.

The spectral models of the FBs can also be divided into mainly two types. First, the hadronic models, in which the gamma-rays are emitted via interactions between cosmic ray (CR) protons and gas phase protons (Crocker & Aharonian 2011; Crocker 2012; Crocker et al. 2014b; Mou et al. 2014, 2015). Second, the leptonic models, in which the low energy photons (either cosmic microwave background or interstellar

* kcsarkar@rri.res.in

radiation field) are energised *in situ* by high energy cosmic ray electrons to produce gamma rays (Su et al. 2010; Mertsch & Sarkar 2011; Sarkar et al. 2015b).

While modelling the gamma rays requires knowledge of the local CR energy density, magnetic field and gas density, and involves some assumptions about the acceleration processes and diffusion of the CRs, the modelling of the bubbles is much simpler in X-rays as it involves only the local gas density and its temperature. From the lack of X-ray emission inside the bubbles it has been suggested that these bubbles are under-dense compared to the surroundings. However, measuring the density inside and outside the bubbles requires a careful fitting of the emission or absorption spectra.

An ideal place to measure the spectra would be the northern polar spur (NPS) where the shell is X-ray bright. However, there have been debates over the actual distance of the NPS. Early observations suggested that the NPS can be a nearby low density bubble created by the stellar wind from the Scorpio-Centaurus OB association or could be a supernova remnant situated at a distance of few hundred pc (Berkhuijsen, Haslam and Salter 1977). Using X-ray observations, however, Sofue (1994); Snowden et al. (1995); Lallement et al. (2016) found that the NPS feature is heavily absorbed towards the Galactic plane requiring a hydrogen column density of $\sim \text{few} \times 10^{21} \text{ cm}^{-2}$ which makes it unlikely to be a nearby feature. Recent observations using *Suzaku* and *XMM-Newton* also found that the spectra can be better explained if the NPS feature is of the ‘Galactic centre origin’ (see section 4.3 of Kataoka et al. (2013) for a detailed discussion). Another recent observation by Gu et al. (2016) of the OVIII Ly- α to Ly- β ratio also supported the ‘Galactic centre origin’ of the NPS (Sofue 1977, 2000; Bland-Hawthorn & Cohen 2003; Sarkar et al. 2015b; Sofue 2016). Also it would be a *dramatic coincidence* that the inner edge of the NPS traces the outer edge of the FBs even at high latitudes if the NPS is not related to the FBs.

Individual pointings towards NPS, therefore, have been used several times to estimate the post shock temperature of the FBs. Observations by Snowden et al. (1995); Kataoka et al. (2013); Gu et al. (2016) suggested that the temperature of the NPS is $\sim 0.25 - 0.3 \text{ keV}$ corresponding to a Mach number (\mathcal{M}) of ~ 1.5 , considering the halo temperature $\approx 2 \times 10^6 \text{ K}$ (estimated from the OVIII to OVII line ratio (Miller & Bregman 2015)). This suggests a star formation driven origin for the FBs (since the stronger AGNW would produce a stronger shock with $\mathcal{M} \gg 1$). However, in a recent observation of the OVIII to OVII line intensity ratio Miller & Bregman 2016, (hereafter, MB16) found that the sight-lines passing through FBs and the surroundings (except the NPS) have a temperature $\approx 5 \times 10^6 \text{ K}$. This let them to conclude that the shock is because of an AGN activity at the Galactic centre and the age of the FBs is $\sim 4 \text{ Myr}$. This differs from other estimates of a lower temperature and a weaker shock, and therefore a longer age of the FBs.

In this paper, we perform 2D hydrodynamical simulations of both star formation driven and accretion wind driven bubbles in a realistic MW gravity and a self consistent halo

gas which is also close to the observed density distribution. We generate projected OVIII to OVII line intensity maps and ratio towards the FBs for a range of injected luminosities and compare them with the observations of MB16. Based on our simulated intensity maps, we constrain the age of the FBs and the strength of the star formation or the accretion wind/ jet activity at the Galactic centre. We also discuss the effects of conduction and the electron-proton equilibration time-scale on our results.

The paper is organised as follows. Section 2 discusses the choice of dark matter and the disc potential and the hydrostatic hot halo gas. The simulation details and other code parameters are explained in section 3. In section 4 we discuss the tool for projecting our 2D simulation results into a surface brightness map of OVIII to OVII line ratio at the Solar location. We present our results in section 5 and finally discuss the implications of the results in section 6.

2 GALACTIC HALO DISTRIBUTION

One issue while modelling the FBs is the density and temperature distribution of the Galactic halo gas which carries crucial information about the soft X-ray background and also determines the shape and speed of any shock travelling through it. Because of our off-centred location, which is $\sim 8.5 \text{ kpc}$ away from the Galactic centre, it is in principle possible to determine the density distribution of the halo. However, there is a split in the opinion as to the correct density distribution. Based on ram pressure stripping of the dwarf satellites, the density has been estimated to be $\sim 1.3 - 3.8 \times 10^{-4} \text{ m}_p \text{ cm}^{-3}$ within 50–90 kpc (Gatto et al. 2013), whereas, based on the distribution of the OVII and OVIII lines, Miller & Bregman (2015) find

$$n(r) = n_0 \left(1 + (r/r_c)^2\right)^{-3\beta/2} \quad (1)$$

with $\beta = 0.5$, $n_0 r_c^{3\beta} = 1.35 \times 10^{-2} \text{ cm}^{-3} \text{ kpc}^{3\beta}$ and $r_c < 5 \text{ kpc}$, which predicts a higher density at the same distance range. A probable solution is that the metallicity of the halo is gradually decreasing with radius. Therefore, a higher density is not apparent in OVII or OVIII line emission (Troitsky et al. 2016). However, there is much to be worked out before making any firm conclusion.

In this paper we assume that the hot halo gas (isothermal at temperature, $T_{\text{halo}} = 2 \times 10^6 \text{ K}$) is in hydrostatic equilibrium with the gravity of the dark matter, the disc stars and the bulge. For the dark matter, we use NFW gravity (Navarro et al. 1996), with an added core to ensure finite dark matter density at $r = 0$,

$$\Phi_{\text{DM}} = -\frac{GM_{\text{vir}}}{f(c)} \frac{\log(1 + \sqrt{r^2 + d^2}/r_s)}{\sqrt{r^2 + d^2}}. \quad (2)$$

Here, M_{vir} is the dark matter mass, $f(c) = \log(1+c) - c/(1+c)$ with c as the concentration parameter of the dark matter distribution, r_s is the scale radius, d is the core radius. For the disc gravity, we use the Miyamoto & Nagai potential

parameters	values
$M_{\text{vir}}(M_{\odot})$	1.2×10^{12}
$M_{\text{disc}}(M_{\odot})$	6×10^{10}
$M_{\text{disc}}(M_{\odot})$	2×10^{10}
$T_{\text{halo}} \text{ (K)}$	2×10^6
c	12
$r_s \text{ (kpc)}$	21.5
$a \text{ (kpc)}$	3.0
$b \text{ (kpc)}$	0.4
$d \text{ (kpc)}$	6.0
$\rho_c(0, 0) \text{ (m}_p\text{cm}^{-3})$	1.9×10^{-2}

Table 1. Parameters used for the mass model of our Galaxy. The assumed mass for different components are roughly consistent with the measurements by [McMillan \(2011, 2016\)](#).

([Miyamoto & Nagai 1975](#))

$$\Phi_{\text{disc}} = -\frac{GM_{\text{disc}}}{\sqrt{R^2 + (a + \sqrt{z^2 + b^2})^2}}, \quad (3)$$

where, M_{disc} is the disc mass, R and z are, respectively, the cylindrical radius and height, a and b represent the scale radius and scale height for the disc gravity. To make the gravity realistic near the Galactic centre, we also add a bulge potential of the form

$$\Phi_{\text{bulge}} = -\frac{GM_{\text{bulge}}}{\sqrt{r^2 + a_b^2}}, \quad (4)$$

where, a_b is the scale radius for the bulge.

The hydrostatic density distribution for the combined gravity, $\Phi = \Phi_{\text{DM}} + \Phi_{\text{disc}} + \Phi_{\text{bulge}}$ can, therefore, be written as

$$\rho(R, z) = \rho(0, 0) \exp\left(-\frac{1}{c_s^2} (\Phi(R, z) - \Phi(0, 0))\right), \quad (5)$$

where, $\rho(0, 0)$ is the density at $r = 0$ and $c_s = \sqrt{k_B T / \mu m_p}$ is the isothermal sound speed at temperature T (for a detailed discussion, see [Sarkar et al. \(2015a\)](#)). However, note that unlike S15, we do not use a rotating cold disc component as our focus is to study the interaction of the wind and the halo gas, in particular the outer shock properties. The interaction of the wind with the disc gas effects the formation of cold clumps. These cold clumps, however, will not effect the observed OVII and OVIII properties.

Figure 1 shows the rotation velocity on the $z = 0$ plane for the parameters given in table 1. For comparison with the observations, data from [Bhattacharjee, Chaudhury & Kundu \(2013\)](#) are shown in the same figure. It shows an excellent consistency with the observed rotation curve of the Galaxy.

The gas density distribution that is in hydrostatic equilibrium with the given gravity (Eq. 5) is shown in figure 2. The figure also shows the effect of adding all the gravity components together. In fact, for the given parameters, the equilibrium density distribution shows an excellent match with the standard β -model obtained by [Miller & Bregman \(2015\)](#) (equation 1 and shown by the cyan line in figure 2) with

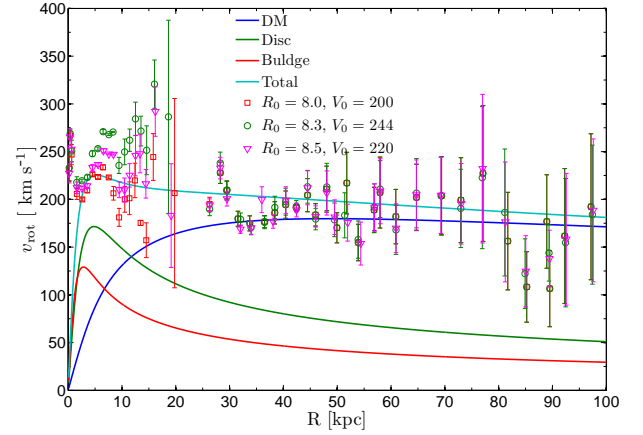


Figure 1. Rotation curve for the assumed gravitational fields for the parameters given in table 1. Data points from [Bhattacharjee, Chaudhury & Kundu \(2013\)](#) have been shown with the errorbars. Different color of the data points represent assumed Solar distance from the Galactic centre (R_0 in kpc) and Solar rotation velocity (V_0 in km s^{-1}).

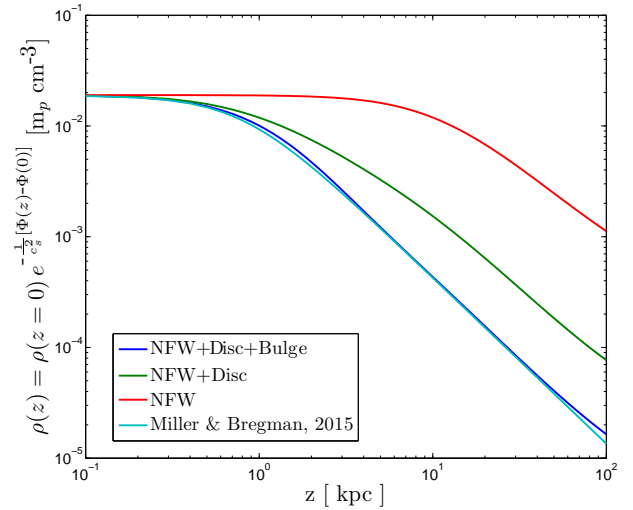


Figure 2. Equilibrium density distribution of the halo gas (Eq. 5) for the parameters given in table 1. The red curve shows the distribution in case of only NFW potential, green curve shows the distribution if the stellar disc is added, blue curve shows the distribution once all the components have been added together. The cyan curve shows the best fitting halo distribution from [Miller & Bregman \(2015\)](#).

$\beta = 0.5$ and $r_c = 0.8$ kpc. Therefore, the hydrostatic equilibrium of MW halo gas distribution can be naturally explained by the total gravitational fields of the MW.

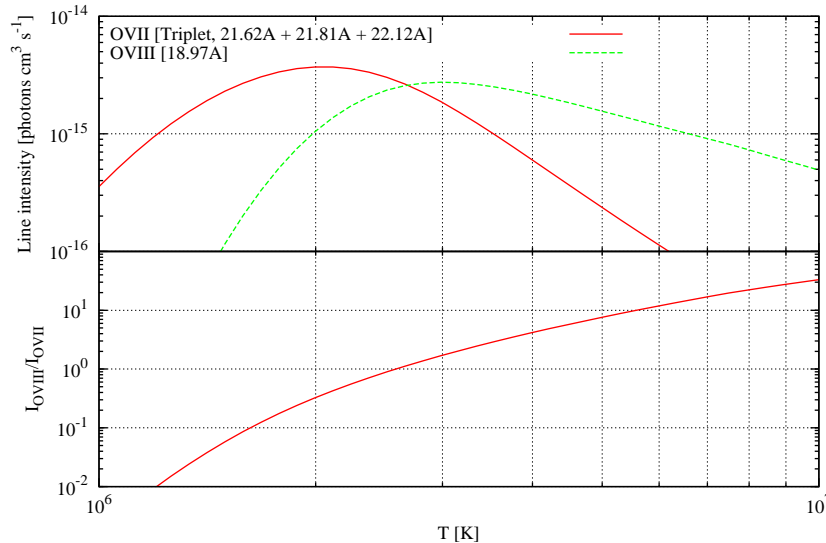


Figure 3. Top panel: Temperature dependence of emissivities of OVII and OVIII lines in units of photons $\text{s}^{-1} \text{cm}^3$ from CLOUDY-C13.04. Bottom panel: Temperature variation of the OVIII to OVII line ratio.

3 SIMULATION DETAILS

The simulations have been performed in a 2-dimensional spherical coordinate using Eulerian grid code PLUTO-v4.0 (Mignone et al. 2007). The computation box extends till 15 kpc in the radial direction and from 0 to $\pi/2$ in the θ -direction. The box has been divided into 256×256 grid cells with uniform grid spacing in both the directions. The inner boundary of the radial direction has been set initially to the static distribution and the outer boundary condition is set to outflow. Both the θ -boundaries have been set to reflective type.

Energy is injected at the inner boundary within some opening angle for all the cases. In reality, the wind will be collimated by the presence of a disc-like structure of the interstellar medium (ISM) or the central molecular zone (CMZ). In case of a SNe driven wind, the energy is mostly thermal and gets deposited into ~ 100 pc region. However, in the presence of the ISM disc, the outgoing wind gets collimated and forms a biconical shape. The amount of collimation depends on the rate at which the energy is being injected from the SNe and the density and pressure structure of the ISM. The accretion wind from the black hole, on the other hand, can be spherical in origin. However, this wind can also be collimated at two stages, first, at the CMZ (Zubovas & Nayakshin 2012) and second, at the ISM disc. The amount of collimation will again depend on the detailed structure of the CMZ and the ISM. Understanding the detailed structure of these components in the central region, as it was at the time of launching the winds, is difficult to do. Since our aim is to study the

outer shock strength for a range of mechanical luminosities, we avoid these issues and consider that the winds have been somehow collimated by the ISM and the CMZ. We also tune the opening angle of the energy and mass injection for each case to roughly match the shape of the contact discontinuity with the FBs. The opening angle for individual runs and other information is provided in table 2.

Although simulations of both star formation driven wind and accretion wind/jet are quite similar, there are certain differences while injecting energy at the inner boundary as mentioned below.

- SNe driven wind: The energy and mass injection radius is set to 100 pc. This radius is assumed to be the transonic point of the wind. Therefore, the velocity at the base (v_{ej}) is kept half of the free wind velocity ($\approx 1000\sqrt{\alpha/\beta}$) (Chevalier & Clegg 1985). Here, $\alpha = 0.3$ is the assumed heating efficiency of the supernovae (SNe) and $\beta = 0.3$ is the mass loading factor from stellar feedback (Leitherer et al. 1999). The pressure is set to be $p = \rho_{ej} v_{ej}^2 / \gamma$, where $\gamma = 5/3$ is the adiabatic index and ρ_{ej} is the density at the base. The mechanical luminosity and the mass injection rate in this case can be written in terms of α and β as

$$\mathcal{L} \approx 3 \times 10^{41} \alpha \text{ SFR}_{\text{M}_{\odot} \text{ yr}^{-1}} \quad (6)$$

and

$$\dot{M}_{\text{inj}} = \beta \text{ SFR}, \quad (7)$$

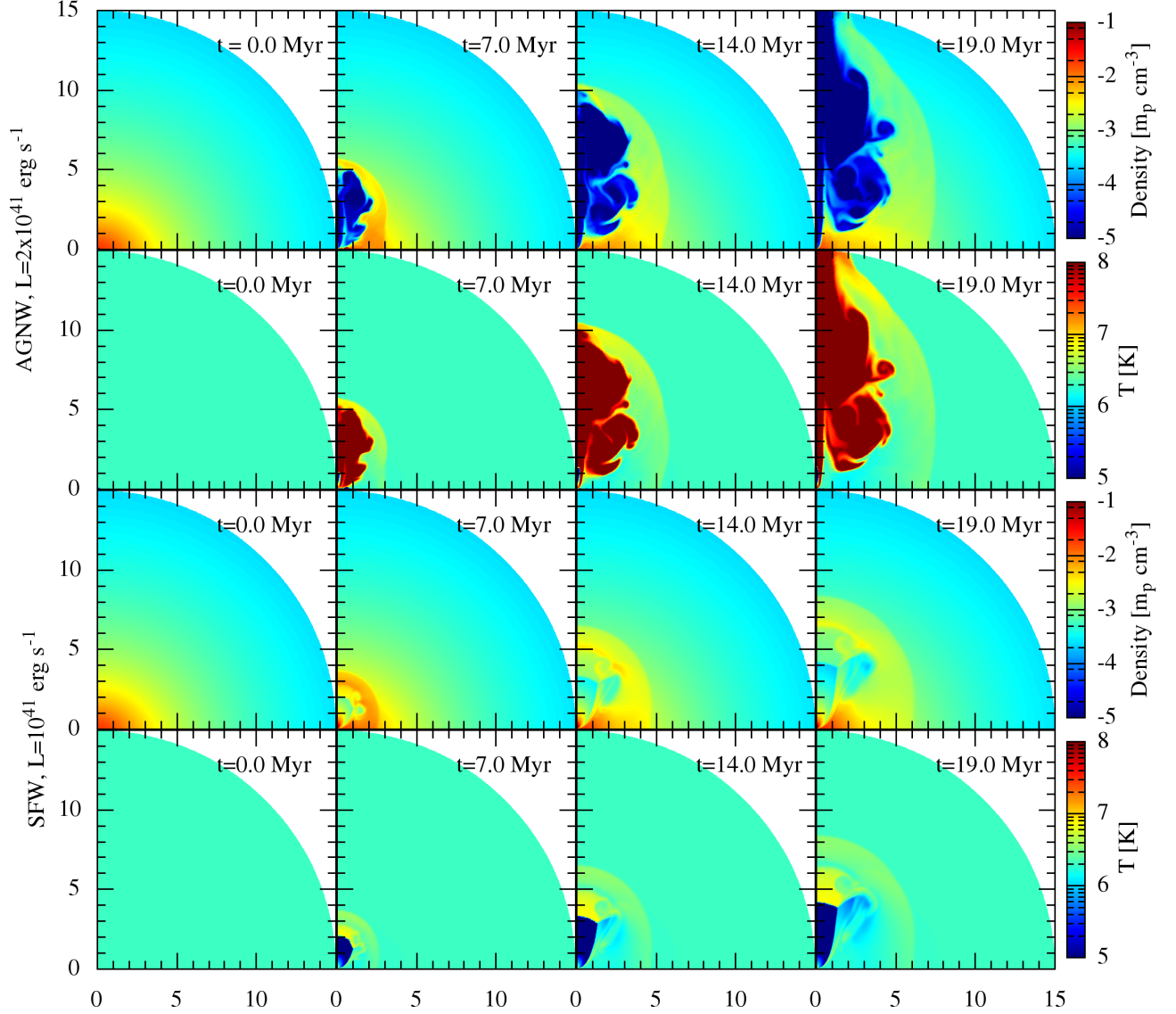


Figure 4. Evolution of density and temperature contours for AGNW and SFW cases. Top two panels represent evolution of an accretion driven wind corresponding to luminosity $\mathcal{L} = 2 \times 10^{41} \text{ erg s}^{-1}$, whereas, bottom two panels represent the evolution of a SF driven wind of luminosity $\mathcal{L} = 10^{41} \text{ erg s}^{-1}$ ($\text{SFR} = 1 \text{ M}_{\odot} \text{ yr}^{-1}$). The X-axis represents the on-plane distance R , and the Y-axis represents the vertical distance, z , from the Galactic disc.

respectively. Therefore, density at the base can be written as

$$\rho_{\text{ej}} = \frac{\mathcal{L}}{2\Omega r^2 v_{\text{ej}}^3}, \quad (8)$$

where, Ω is the solid angle within which the mass and energy are injected.

- **Accretion wind:** In this case, the injection radius is 20 pc. The injection is mostly in the form of kinetic energy and the velocity of the wind is set to be $v_{\text{ej}} = 0.05c$, where c is the speed of light. The density at the base is set to be $= 2\mathcal{L}/\Omega r^2 v_{\text{ej}}^3$ and the pressure of wind is set to be equal to the ISM pressure at that location. However, a low mass injection

Table 2. List of runs and the parameters used in these runs.

Name	Type	Luminosity (erg s ⁻¹)	Half opening angle
A5e40	AGNW	3×10^{40}	60°
A2e41	AGNW	2×10^{41}	45°
A1e42	AGNW	1×10^{42}	45°
S5e40	SFW	3×10^{40}	60°
S7e40	SFW	5×10^{40}	60°
S1e41	SFW	1×10^{41}	45°

rate and high velocity of the AGNW makes the code unstable. In order to bypass this issue, we set a cold ($T = 10^3$ K) and dense ($\rho = 100 \text{ m}_p \text{ cm}^{-3}$) gas sphere extending till 50 pc. In fact, it roughly mimics the cold molecular zone (CMZ) at the Galactic centre. Note that, since we inject the SNe energy at a scale of 100 pc, this gas sphere is not included in those simulations.

4 ANALYSIS TOOLS

4.1 Projection tool

Since we are at the Solar position, ≈ 8.5 kpc away from the Galactic centre, which is roughly comparable to the height (~ 10 kpc) and width (~ 4 kpc) of FBs, the projection effects are important. A special purpose code, called Projection Analysis Software for Simulations (PASS)¹, has been written to project the 2D simulation data to a viewer from the Solar location (assuming axisymmetry). It can also project an 1D profile into a 2D sky map, assuming spherical symmetry of the profile. The surface brightness along any line of sight (l, b) is calculated as

$$I(l, b) = \frac{1}{4\pi} \int_{\text{los}} n^2 \varepsilon(T) dx \quad \text{erg s}^{-1} \text{cm}^{-2} \text{Sr}^{-1}, \quad (9)$$

where, n is the particle density and $\varepsilon(T)$ is the emissivity (erg s⁻¹ cm³) at any local point along the line of sight (LOS). It can also produce mock X-ray spectra along different LOSs assuming plasma emission code MEKAL (Mewe-Kaastra-Liedahl). Since our simulation box only extends till 15 kpc, to produce realistic emission maps, we consider the density distribution extending till 250 kpc, and include a local bubble centred at Sun with a radius of 200 pc, density of $4 \times 10^{-3} \text{ m}_p \text{ cm}^{-3}$ and a temperature of $= 1.2 \times 10^6$ K following MB16.

4.2 Oxygen emission lines

The line emissivities for OVII and OVIII, assumed to be in collisional ionisation equilibrium, have been obtained from

¹ PASS is made public and is available for download at http://www.rri.res.in/~kcsarkar/pages/about_me/codes.html

CLOUDY-C13.04 (Ferland et al. 2013) and are described in figure 3. It is clear from the figure that the OVIII to OVII line ratio is sensitive to the temperature, making it a very useful for temperature diagnostic in the range of 10^6 – 10^7 K.

5 RESULTS

Figure 4 shows the evolution of density and temperature for the AGNW and SFW models. Within the opening angle, they show a typical structure of the wind blown bubble containing free wind, shocked wind and shocked halo gas (Weaver et al. 1977). Note that, the free wind region in case of AGNW is very small and not visible in the density plot because of the colour bar. In a typical wind scenario, the reverse shock appears when the wind ram pressure balances the shocked halo pressure. The reverse shock position can be written as (see equation 12 of Weaver et al. (1977))

$$r_{\text{rs}} \propto \mathcal{L}^{3/10} \rho_0^{-3/10} v_w^{-1/2} t^{2/5}, \quad (10)$$

where \mathcal{L} is the mechanical luminosity and v_w is the free wind velocity, ρ_0 is the background density and t is the time. Here, we have assumed the mass injection rate, $\dot{M} = 2\mathcal{L}/v_w^2$. It is, therefore, clear that the reverse shock in AGNW will be much closer to the centre compared to the SFW for the same luminosity.

One important difference between the AGNW and SFW scenarios is the temperature of the shocked wind. for AGNW, it is much higher ($T_{\text{sw}} \gtrsim 10^8$ K) compared to the SFW ($T_{\text{sw}} \sim 10^7$ K), and the density in AGNW case is much lower ($\rho_{\text{sw}} \sim 10^{-5} \text{ m}_p \text{ cm}^{-3}$) compared to the SFW case ($\rho_{\text{sw}} \sim 10^{-3} \text{ m}_p \text{ cm}^{-3}$). This is because of the following reasons. Assuming that the total energy is released in the form of kinetic energy, the density of the free wind at any radius, r , can be given as

$$\rho_w = 2\mathcal{L}/(\Omega r^2 v_w^3), \quad (11)$$

where, Ω is the wind opening solid angle. The pressure and temperature of the reverse shocked gas are, therefore, given as $P_{\text{sw}} \propto \rho_w v_w^2 = 2\mathcal{L}/(\Omega r^2 v_w)$ and $T_{\text{sw}} \propto v_w^2$, respectively. This means that a high velocity wind will always create a higher temperature and low density shocked wind.

It is clear from the above arguments that knowledge of the density structure inside the FBs will help to distinguish between the AGNW and SFW cases. In fact, the best fit model of MB16 (their figure 10a) prefers a high density ($\sim 10^{-3} \text{ m}_p \text{ cm}^{-3}$) interior of the FBs, which is possible if either SF luminosity is $\sim 10^{41} \text{ erg s}^{-1}$ (SFR $\sim 1 \text{ M}_\odot \text{ yr}^{-1}$) or AGNW luminosity is $\sim 5 \times 10^{44} \text{ erg s}^{-1}$ ($\approx 0.8 \mathcal{L}_{\text{edd}}$, for a black hole mass of $4 \times 10^6 \text{ M}_\odot$), assuming $r_{\text{rs}} \sim 2$ kpc and $\Omega = 2\pi$ in equation 11. *This is a consequence of the fact that the AGNWs are much less mass loaded compared to the SFWs.*

In AGNW case, it is hard to produce the fitted OVIII volume emissivity (shown in figure 10d of MB16) inside the bubble since the emissivity of OVIII lines at $\gtrsim 3 \times 10^8$ K is $n^2 \varepsilon(T) \sim 10^{-28} \text{ photons s}^{-1} \text{ cm}^{-3}$, assuming $n \sim 10^{-5} \text{ cm}^{-3}$ and $\varepsilon(3 \times 10^8 \text{ K}) \sim 2 \times 10^{-18} \text{ photons s}^{-1} \text{ cm}^3$ (see figure 3).

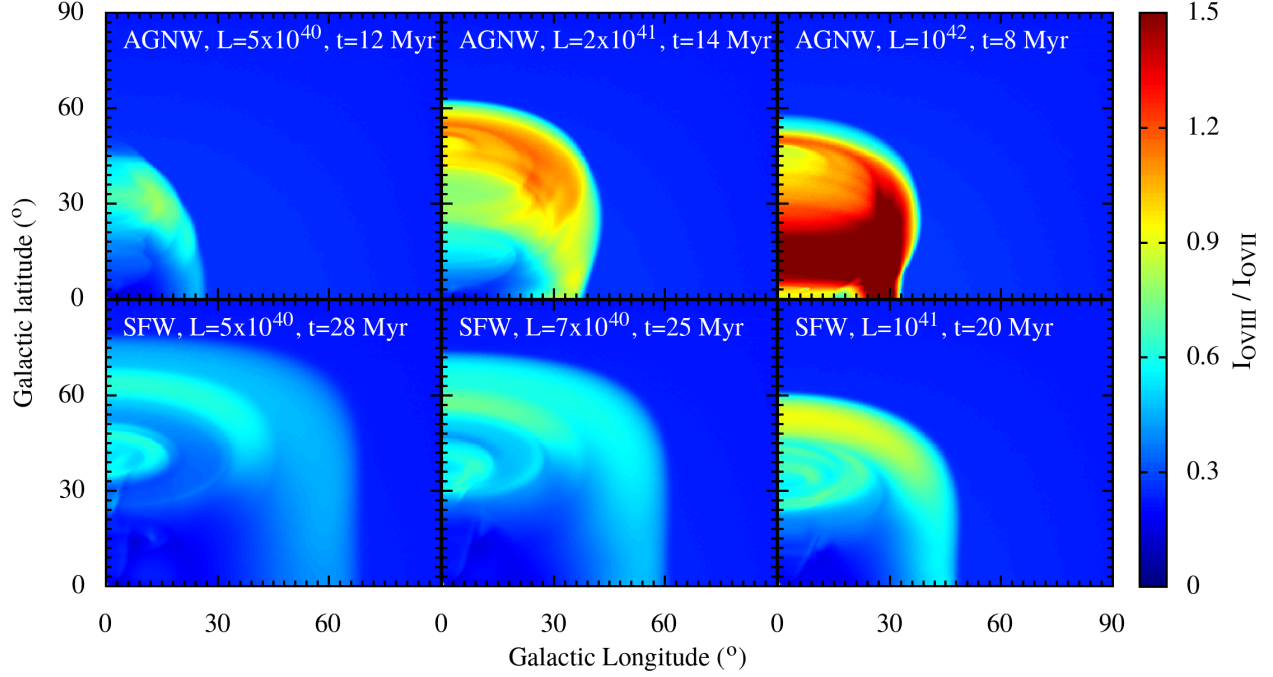


Figure 5. Simulated OVIII to OVII line ratio map for all the runs mentioned in table 2. Note that, AGNW with $\mathcal{L} = 5 \times 10^{40}$ erg s $^{-1}$ creates a tunnel along rotation axis and escapes the system without much interaction with the CGM gas after 12 Myrs. Therefore, the produced bubble is much smaller than the observed one.

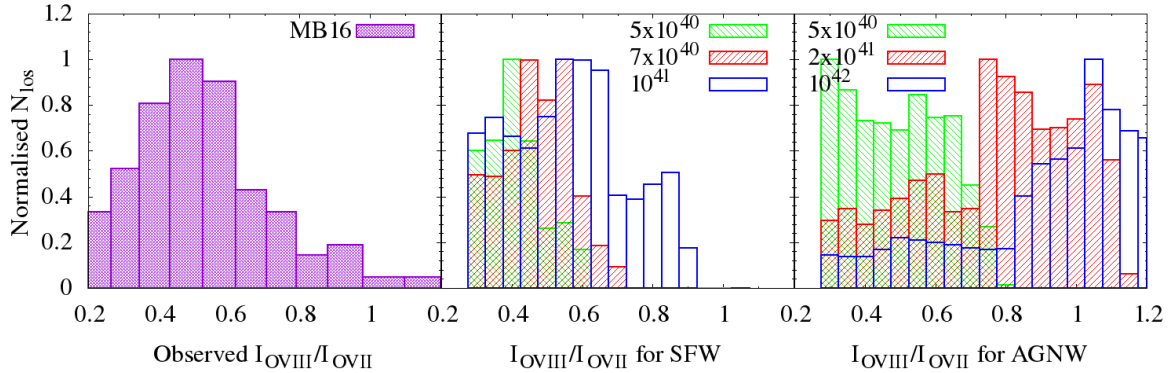


Figure 6. Normalised histograms of the OVIII to OVII line ratio. The observed values of MB16 are shown in the left panel. The middle and the right panels show the obtained line ratio histograms for the SFW and AGNW cases, respectively. Different mechanical luminosities (given in erg s $^{-1}$) are represented by different box styles. All the N_{los} values are normalised with respect to the maximum number of LOSs obtained in corresponding mechanical luminosities.

This value is clearly ~ 7 orders of magnitude lower than the fitted one. Conduction can, in principle, increase the density inside the bubble and reduce the temperature. Tests with 1D simulations including conduction (see section 6.3) show that the temperature of the bubble (i.e. inside the contact discontinuity, which in this case is at ≈ 5 kpc) is $\gtrsim 10^7$ K and the density is $\lesssim 5 \times 10^{-4}$ m $_p$ cm $^{-3}$. Therefore, the volume emissivity can increase to 2×10^{-24} photons s $^{-1}$ cm $^{-3}$, which

is still ~ 3 orders of magnitude lower than the fitted value $\sim 10^{-21}$ photons s $^{-1}$ cm $^{-3}$. However, we should keep in mind that estimating the emissivity inside the low density bubble is a complex process as it may be contaminated by the shell emission and may not be distinguishable by a simple fitting of a bubble and a shell.

On the other hand, for SFW, the bubbles density $n \sim 10^{-3}$ cm $^{-3}$ and the bubble temperature is $\sim 10^6 - 10^7$ K, for

which the OVIII volume emissivity is $\sim 4 \times 10^{-22}$ photons $\text{s}^{-1} \text{cm}^{-3}$ (assuming $\varepsilon = 10^{-15}$ photons $\text{s}^{-1} \text{cm}^3$) which is much closer to the fitted value.

In case of the intensity ratio between OVIII and OVII lines, the comparison becomes non-trivial as the LOS may consist of gas at different temperatures and therefore can have different line ratios compared to a single temperature medium. For direct comparison with the observations, it is necessary to consider the effects of any intervening or background medium. We, therefore, use our projection software PASS to produce the line intensity maps including the effects of the local bubble and the halo medium extending till ~ 250 kpc as explained in section 4.1.

While producing line emission maps, it is necessary to know the age of the FBs because the forward shock velocity and hence the shocked halo temperature depends on time as

$$v_{\text{fs}} \approx \frac{3}{5} \left(\frac{\mathcal{L}}{\rho_0} \right)^{1/5} t^{-2/5}, \quad (12)$$

where, the symbols have same meanings as in equation 10. Therefore, it is necessary to know the region where the gamma-rays are produced. It could either be the forward shock or the reverse shock (Lacki 2014) or the contact discontinuity (Mou et al. 2015; Crocker et al. 2014b) or the region within the contact discontinuity (Mertsch & Sarkar 2011; Sarkar et al. 2015b). Here, we follow Sarkar et al. (2015b) and assume that the gamma-rays originate from the region within the contact discontinuity. Therefore, we, set the age of FBs when the contact discontinuity reaches latitude $b \approx 50^\circ$ (height of the FBs). Since the forward shock radius $r_{\text{fs}} \approx (\mathcal{L}t^3/\rho_0)^{1/5}$, this age of the FBs is different for different luminosities and is shown in the corresponding panels in figure 5.

Figure 5 shows the OVIII to OVII line ratio maps for AGNW (top panel) and SFW (bottom panel) models obtained at the age of the FBs (as explained above) for different luminosities. It shows that the line ratio is highest on the top of the bubble where the shock is the strongest and becomes lower on the either sides where the shock is weaker, a typical behaviour for a bow shock. Notice that in some cases the emission forms a shell-like feature, this is because the low density interior does not contribute much to the line ratio and most of the emission comes from the shell-like shocked halo gas.

For a better comparison with the observed data, in Figure 6, we also plot histograms of the OVIII to OVII line ratios for different mechanical luminosities and injection scenarios. In this figure we intentionally excluded all the LOSs that have line ratio less than 0.3 to avoid contamination from the halo gas.

It is clear from the above figures that only $\mathcal{L} \sim 7 \times 10^{40}$ erg s^{-1} in case of SFW and $\mathcal{L} \sim 5 \times 10^{40}$ erg s^{-1} in case of AGNW match the observed line ratio. A higher (lower) luminosity in either case produces a line ratio that is more (less) than the observed ones. We, therefore, can constrain the mechanical luminosity of the source of the FBs to be $\mathcal{L} \sim 7 \times 10^{40}$ erg s^{-1} for the star formation scenario and $\mathcal{L} \sim 5 \times 10^{40}$

erg s^{-1} for the Accretion wind scenario. However, for such low luminosity AGN, the wind is not properly thermalised and the morphology of the contact discontinuity differs from the observed shape of FBs.

The post shock temperature for the SF case corresponds to $\sim 3 \times 10^6$ K, whereas, for the AGNW case, the temperature is $\sim 6 \times 10^6$ K at $\theta = 0$ axis and falling rapidly to $\sim 3 \times 10^6$ K at an angle of 20° from the rotation axis. This estimate of temperature is consistent with the measurements by Kataoka et al. (2013); Gu et al. (2016) at the NPS. The similarity of the NPS temperature to the other parts of the FBs is another *dramatic coincidence* that has to be explained if the NPS is not related to the FBs.

6 DISCUSSIONS

6.1 Effects of cosmic ray and magnetic pressure

So far in our simulations we have not considered cosmic ray or magnetic pressure on the dynamics of the gas. However, it has been shown that the cosmic ray pressure and the magnetic pressure can contribute approximately half of the thermal energy of the Galactic wind (Sarkar et al. 2015b). Therefore, the required energy solely from star formation process to drive the FBs is $\sim 5 \times 10^{40}$ erg s^{-1} , which corresponds to $\sim 0.5 M_\odot \text{yr}^{-1}$ consistent with the estimates by Sarkar et al. (2015b). The estimated mechanical luminosity required only from a SFW wind is, however, dependent on the fraction of the thermal energy in CRs and in the magnetic field.

6.2 Enhanced emission beyond FBs

One point to notice in Figure 5 is that the line ratio is enhanced beyond the edge of the FBs (extended till 50° in latitude and $\sim 20^\circ$ in longitude). Interestingly, such an extended emission (till $\sim 60^\circ$ in both longitude and latitude) in OVIII intensity and the OVIII to OVII line ratio is also noticed in the observations (see figure 4 and 6 of MB16). We speculate that this extended emission can be an indication of the forward shock travelling through the circumgalactic medium.

6.3 Effects of conduction

Conduction also can effect the dynamics and the density and temperature profiles of the bubble. We, therefore, use isotropic conduction module given in PLUTO. The heat flux is calculated as

$$F = \frac{F_{\text{sat}}}{F_{\text{sat}} + F_{\text{class}}} F_{\text{class}}, \quad (13)$$

where, $F_{\text{class}} = 5.6 \times 10^{-7} T^{5/2} \nabla T$ is the classical thermal conduction flux. In cases where the temperature gradient is very large, the above equation also takes care of the saturation effects by including $F_{\text{sat}} = 5\phi\rho c_{\text{iso}}^3$, where, $\phi = 0.3$ and c_{iso} is the isothermal sound speed. The effects of conduction are, therefore, more in the case of AGNW because of the high

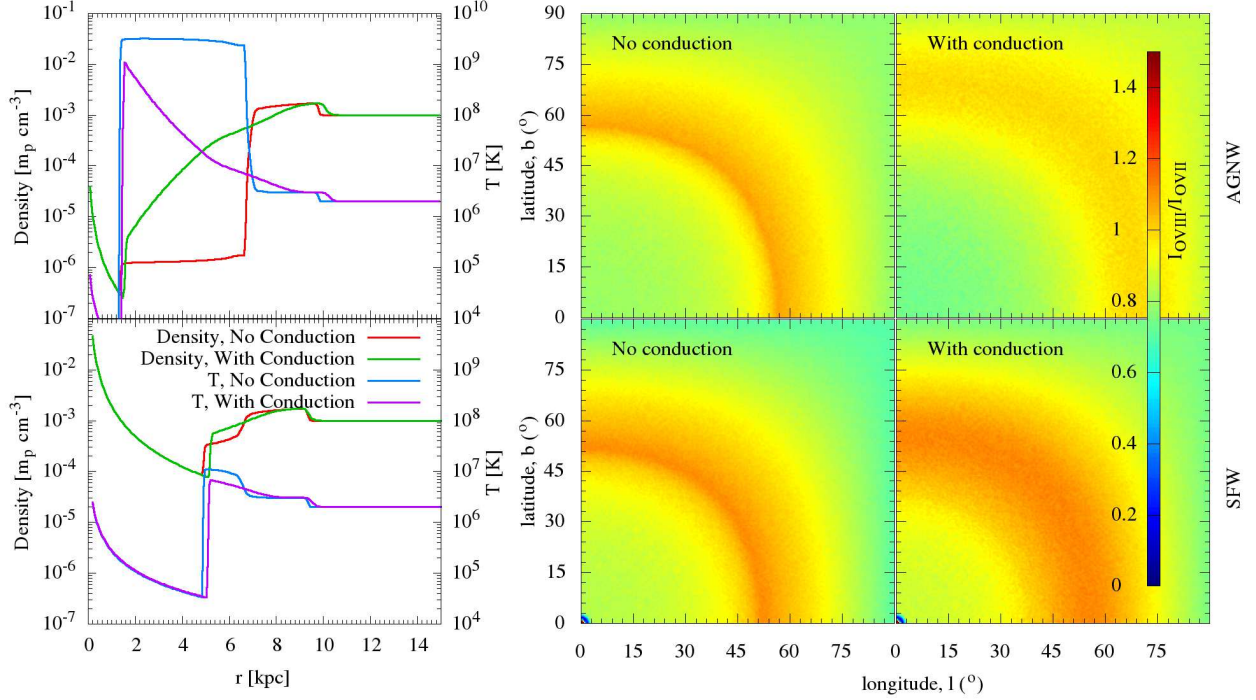


Figure 7. Effects of conduction for one dimensional test runs of AGNW (top panel) and SFW (bottom panel) at 20 Myr. The one dimensional density (left axis) and temperature (right axis) profiles for runs with/without conduction have been shown in the left panel of the figure. The corresponding effects on the OVIII to OVII line ratios have been shown in the middle and right panels. The colour represents the OVIII to OVII line intensity ratio. While calculating the line intensity ratio, we kept the box only till 15 kpc to avoid contribution from the background halo gas.

temperature compared to the SFW case. However, incorporation of the thermal conduction in AGNW runs makes the structure of the outer shock highly elongated along the $\theta = 0$ axis and forms a very thin jet like feature. In reality, conduction can get suppressed due to the presence of magnetic field. A proper treatment will require incorporation of anisotropic conduction which is beyond the scope of this work. Instead, we present one-dimensional test runs with/without conduction to understand the effects of conduction. However, we alert the reader that these runs should be taken only as indicative of the actual situation. Moreover, electrons and protons may not have the same temperature behind the shock, as the Coulomb interaction time-scale between the two can be long, as discussed in section 6.4.

Figure 7 shows the 1D runs with/without conduction. The upper panel shows the runs for AGNW and the lower panel shows the runs for SFW for a mechanical luminosity $= 2 \times 10^{41} \text{ erg s}^{-1}$ at 20 Myr. The density and temperature profiles for the SFW case show little variation if conduction is present. The effects are large in case of AGNW because of the large temperature inside the bubble. Although the outer shock structure remains almost same, the structure of the density and temperature inside the contact discontinuity (≈ 5 kpc) changes by almost two orders of magnitude. To compare

the integrated line intensity ratio, we put these 1D bubbles at the Galactic centre and produce the line intensity maps as shown by the colour contours in middle (without conduction) and right panel (with conduction) of Figure 7. The contours show little variation in the line intensity ratio even if conduction is included. This is because the contribution to the line intensity mainly comes from the outer shock which remains almost unaffected by the conduction. Therefore, the line intensity maps presented in Figure 5 are likely to be unaffected by conduction.

One aspect, however, immediately improves in case of AGNW is the OVIII emissivity inside the contact discontinuity. As mentioned earlier, conduction can increase the OVIII emissivity in this case to $\sim 2 \times 10^{-24} \text{ photons s}^{-1} \text{ cm}^{-3}$. The exact value however depends on the definition of the bubble i.e. the region where the gamma-ray emission is generated. This will involve careful modelling of the diffusion of CR particles in this scenario.

Also, notice that the effects of conduction have been overestimated in these simulations. Presence of the magnetic field will decrease the effects of conduction. However, a simple estimate of the average OVIII emissivity in the region within the outer shock shows that the average emissivity is $\sim 4 \times 10^{-21} \text{ photons s}^{-1} \text{ cm}^{-3}$ in all the cases i.e. with/without conduc-

tion in AGNW/SFW cases. Since we are looking at projected emission, even the bubble region emits significantly in OVIII because of the outer shock along the sightline. Therefore, it is difficult to distinguish between AGNW and SFW using the OVIII emissivity fitted by MB16.

6.4 Electron-proton energy equilibration

Eq. 13 assumes that electrons and protons have the same temperature. This assumption is valid only when the electron-proton energy exchange time due to Coulomb collisions is short enough. This time-scale is (using Eq. 5-31 in [Spitzer 1956](#)),

$$t_{eq} \sim 0.25 \text{ Myr } T_6^{3/2}/n_{-3}, \quad (14)$$

where, T_6 is the electron temperature in the units of 10^6 K and n is the proton/electron number density. The corresponding length scale required to attain equilibrium is $l_{eq} = v t_{eq} \sim 75 T_6^{3/2}/n_{-3} \text{ pc}$ for $v = 300 \text{ km s}^{-1}$ (v is the flow velocity). Thus, for the outer shock density and temperature (for both SFW and AGNW scenarios) t_{eq} is shorter than the age of FBs, and therefore the electron and proton temperature behind the outer shock can be treated as equal.

For the much stronger reverse shock in the AGNW scenario (top-left panel of Fig. 7), the post-shock temperature is $\sim 10^9$ K and density is $\sim 10^{-6} \text{ cm}^{-3}$. The electron-proton energy exchange time for these parameters is $\sim 10^7$ Myr! For the SFW scenario (top-left panel of Fig. 7) t_{eq} is ~ 15 Myr, and even here the assumption of equal electron and proton temperature is only marginally valid. Thus the strong reverse shock is in the collisionless regime, and the electron temperature is expected to be much smaller than the proton temperature (e.g., see Fig. 2 in [Ghavamian et al. 2007](#)). Therefore, the effects of thermal conduction are exaggerated in the top panels of Figure 7, and in reality the density in the bubble (particularly for the AGNW scenario) may be closer to the case without conduction.

For a strong outer shock ($M \sim 10$, representative of a high luminosity wind) the forward shock temperature can become $T \sim 10^8$ K for which $t_{eq} \sim 100$ Myr (Eq. 14). In such a case, the electrons are expected to be much cooler than the protons and, therefore, the outer shock strength may be underestimated. We can estimate the maximum luminosity for which our analysis, which hinges on equal electron and proton temperature, of the outer shock strength is valid. The outer shock temperature for a mechanical luminosity \mathcal{L} can be written as

$$T_{\text{shock}} = 2.5 \times 10^7 \mathcal{L}_{42}^{2/5} n_{-3}^{-2/5} t_{\text{dyn,Myr}}^{-4/5} \text{ K}, \quad (15)$$

where, $\mathcal{L} = 10^{42} \mathcal{L}_{42} \text{ erg s}^{-1}$ and $t_{\text{dyn,Myr}}$ is the time in units of Myr which is given by

$$t_{\text{dyn,Myr}} = 11 R_{10\text{kpc}}^{5/3} n_{-3}^{1/3} \mathcal{L}_{42}^{-1/3}. \quad (16)$$

Here, $R = 10 R_{10\text{kpc}}$ kpc is the outer shock radius. Therefore, we can write Eq. 14 as

$$t_{\text{eq,Myr}} \sim 1.74 \mathcal{L}_{42} n_{-3}^{-2} R_{10\text{kpc}}^{-2}. \quad (17)$$

Now, for the electron and proton temperature to be equal, $t_{eq} \lesssim t_{\text{dyn}}$, which means

$$\mathcal{L} \lesssim 4 \times 10^{42} n_{-3}^{7/4} R_{10\text{kpc}}^{11/4} \text{ erg s}^{-1}. \quad (18)$$

Therefore, our analysis of the outer shock strength is valid for $\mathcal{L} \lesssim 4 \times 10^{42} \text{ erg s}^{-1}$. A higher mechanical luminosity ($\gtrsim 4 \times 10^{42} \text{ erg s}^{-1}$) winds can, in principle, have a lower electron temperature at the outer shock and produce OVIII/OVII line intensity similar to the low luminosity winds. However, it is well known for accretion power that the black holes do not produce mechanical energy $\gtrsim 1\%$ of L_{edd} ([Churazov et al. 2005](#)). For the GCBH, this limits the maximum available mechanical energy to be $\lesssim 5 \times 10^{42} \text{ erg s}^{-1}$. Therefore, our estimate of a weak outer shock strength is the only possible solution for explaining the OVIII to OVII line ratio.

6.5 AGNW vs. SFW

In case of a SFW, the obtained mechanical luminosity ($5 \times 10^{40} \text{ erg s}^{-1}$) corresponds to a SFR $\sim 0.5 M_{\odot} \text{ yr}^{-1}$ (see equation 6). Notice that this value is slightly larger compared to the observations by [Yusuf-Zadeh et al. \(2009\)](#), who found SFR $\sim 0.1 M_{\odot} \text{ yr}^{-1}$. However, recent discovery of a ~ 100 pc molecular ring can, in principle, host a higher SFR. Also, note that the required rate of SFR depends on the exact amount of CR and magnetic energy density inside the bubbles.

On the other hand, linear polarisation of $\gtrsim 150$ GHz emission, and IR and X-ray variability of the Sgr A* suggests that the current accretion rate of the GCBH is $\sim 10^{-9} - 10^{-7} M_{\odot} \text{ yr}^{-1}$ ([Quataert & Gruzinov 2000](#); [Agol 2000](#); [Yuan, Quataert & Narayan 2003](#); [Marrone et al. 2006](#)), which corresponds to a mechanical luminosity of $\sim 5 \times 10^{36-38} \text{ erg s}^{-1}$, assuming an efficiency factor of 0.1 (see section 1). However, in order to explain the X-ray luminosity around the Sgr A*, it has been suggested that the past accretion rate of the GCBH could have been 10^{3-4} higher than the present day accretion rate ([Totani et al. 2006](#)). This means that the GCBH mechanical luminosity was $\lesssim 5 \times 10^{39-41} \text{ erg s}^{-1}$. Although there is a large uncertainty in the past mechanical luminosity, it is surprisingly close the required rate of $5 \times 10^{40} \text{ erg s}^{-1}$. Also, we must note that the black hole activity is highly variable in time and it is the average mechanical luminosity that should be considered. One issue with such a low luminosity AGNW, however, remains. It is not able to produce the observed bubble morphology and creates a much elongated bubble structure than observed.

In this paper, though we constrain the mechanical luminosity for the source driving the FBs, the degeneracy between the SFW and the AGNW models still remains. One way to distinguish between these two models is probably the kinematics of the hot gas inside the bubbles. As noted by [Sarkar et al. \(2015b\)](#), the velocity range of the hot wind for SFW can be $\sim \pm 600 \text{ km s}^{-1}$. However, in case of AGNW, This velocity range will be much higher. Another way is to measure the temperature along the outer edge of the FBs. In AGNW case, the outer shock is relatively more anisotropic than the SFW case. This is because the AGNW is completely kinetic energy

driven and has a large velocity anisotropy perpendicular to the disc thus producing a strong bow shock and, therefore, producing a somewhat anisotropic shock temperature. The SFW, on the other hand, has a large fraction of energy in the form of internal energy and hence the outer shock structure is more isotropic (see Figure 4). However, one must note that measuring the temperature along the edge of the FBs using the OVIII to OVII line ratio is likely to be contaminated by the detailed structure of the MW halo gas as the contribution from the background halo gas is non-negligible.

7 SUMMARY

We have explored different driving mechanisms to inflate the FBs: one, a central black hole driven wind (AGNW), and second, a star formation driven wind (SFW). The winds have been launched at the Galactic centre and have been allowed to propagate through a realistic distribution of the MW halo gas. We compare our numerical simulations of SNe and AGN wind models with the best fit model of Miller & Bregman (2016). We find that irrespective of the driving mechanism - AGNW or SFW, the total luminosity required to produce the observed OVIII to OVII line ratio is $\approx 5 - 7 \times 10^{40} \text{ erg s}^{-1}$. The given luminosity also constrains the age of the FBs to be $\approx 15\text{--}20 \text{ Myr}$.

The shocked halo temperature is estimated to be $\approx 3 \times 10^6 \text{ K}$ in most of the forward shock. For a weak shock travelling through a $2 \times 10^6 \text{ K}$ halo gas, this temperature would correspond to a shock velocity of $\sim 300 \text{ km s}^{-1}$. This value is slightly lower compared to the estimates by Miller & Bregman (2016) who found the temperature to be $\approx 5 \times 10^6 \text{ K}$ based on the same data. Our temperature estimate is, however, consistent with the temperature measurements by Kataoka et al. (2013) and Gu et al. (2016) at the NPS, which indicates that the NPS has likely originated from the same activity that gave rise to the FBs.

ACKNOWLEDGEMENTS

It is a pleasure to thank David Eichler for helpful discussions on the electron-proton equilibration temperature. We thank Yoshiaki Sofue and Tomonori Totani for useful comments on the draft. KCS thanks Saurabh Singh for helps in debugging PASS. This work is partly supported by an India-Israel joint research grant (6- 10/2014[IC]).

REFERENCES

- Ackermann A., et al. , 2014, *ApJ*, 793, 64
 Agol E., 2000, *ApJ*, 538, L121
 Berkhuijsen E. M., Haslam C. G. T., Salter C. J., 1977, *A&A*, 14, 252B
 Bhattacharjee P., Chaudhury S., Kundu S., 2013, *ApJ*, 785, 63
 Bland-Hawthorn J., Cohen M., 2003, *ApJ*, 582, 246
 Carretti E., Crocker R. M., Staveley-Smith L., et al. 2013, *Nature*, 493, 66
 Chevalier R. A., Clegg A. W., 1985, *Nature*, 317, 44
 Churazov E., Sazonov S., Sunyaev R., Forman W., Jones C., Böhringer H., 2005, *MNRAS*, 363, L91
 Crocker R. M. & Aharonian F., 2011, *PRL*, 106, 101102
 Crocker R. M., 2012, *MNRAS*, 423, 3512
 Crocker, R. M., Bicknell, G. V., Carretti, E., Hill, A. S., Sutherland, R. S. 2014, *ApJL*, 79, L20
 Crocker, R. M., Bicknell, G. V., Taylor, A. M., Carretti, E., 2014, arXiv: 1412.7510
 Ferland G. J., Proter R. L., van Hoof P. A. M., Williams R. J. R., et al. , 2013, *RMexAA*, 49, 137
 Gatto A., Fraternali F., Read J. I., Marinacci F., Lux H., Walch S., 2013, *MNRAS*, 433, 2749
 Ghavamian P., Laming J. M., Rakowski C. E. 2007, *ApJ*, L69
 Gu L., Mao J., Costantini E., Kaastra J., 2016, arxiv:1607.08334
 Guo F. & Mathews W. G., 2012, *ApJ*, 756, 181
 Kataoka, J., Tahara, M., Totani, T., Sofue, Y. et al. 2013, *ApJ*, 779, 57
 Lacki B. C. 2014, *MNRAS*, 444, L39
 Lallement R., Snowden S., Kuntz K. D., Dame T. M., Koutroumpa D., Grenier I., Casandjian J. M., 2016, arxiv:1609.03813
 Leitherer C., 1999, *ApJSS*, 123, 3
 Marrone D. P., Moran J. M., Zhao J-H., Rao R., 2006, *JPhCS*, 54, 354
 McMillan P. J., 2011, *MNRAS*, 414, 2446
 McMillan P. J., 2016, arxiv:1608.00971
 Mertsch, P., Sarkar, S., 2011, *PRL*, 107, 091101
 Mignone, A., Bodo, G., Massaglia, S., Matsakos, T., Tesileanu, O., Zanni, C., Ferrari, A., 2007, *ApJSS*, 170, 228
 Miller M. J., Bregman J. N., 2015, *ApJ*, 800, 14
 Miller M. J., Bregman J. N., 2016, arxiv:1607.04906
 Miyamoto M., Nagai R., 1975, *PASJ*, 27, 533
 Molinari S. et al. , 2011, *ApJ*, 735, L33
 Mou, G., Yuan, F., Bu, D., Sun, M., Su, M. 2014, *ApJ*, 790, 109
 Mou G., Yuan F., Gan Z., Sun M. 2015, *ApJ*, 811, 37
 Munro M. P., Baganoff F. K., Bautz M. W. et al. 2004, *ApJ*, 613, 326
 Navarro J., Frenk C. F., White S., 1996, *ApJ*, 462, 563
 Quataert E., Gruzinov A., 2000, *ApJ*, 545, 842
 Rybicki G. B., Lightman A. P., 1979, *Radiative processes in astrophysics*, Wiley
 Sarkar K. C., Nath B. B., Sharma P., Shchekinov Y., 2015, *MNRAS*, 448, 328
 Sarkar K. C., Nath B. B., Sharma P., 2015, *MNRAS*, 453, 3827
 Snowden S. L. et al. 1995, *ApJ*, 454, 643
 Sofue Y., 1977, *A&A*, 60, 327
 Sofue Y., 1994, *ApJ*, 431, L91
 Sofue Y., 2000, *ApJ*, 540, 224
 Sofue Y., Habe A., Katoka J., Totani T., et al. , 2016, *MNRAS*, 459, 108

- Spitzer, L., Physics of Fully Ionized Gases, New York: Interscience Publishers, 1956
- Su M., Slatyer T. R., Finkbeiner D., 2010, ApJ, 724, 1044
- Totani T, 2006, PASJ, 58, 965
- Troitsky S., 2016, 1607.05442
- Weaver R., McCray R., Castor J., Shapiro P., Moore R., 1977, ApJ, 218, 377
- Yang H.-Y. K., Muszkowski M., Ricker P. M., Zweibel E., Lee D., 2012, ApJ, 761, 185
- Yuan F., Quataert E., Narayan R., 2003, ApJ, 598, 301
- Yusuf-Zadeh F. et al. , 2009, ApJ, 702, 178
- Zubovas K. & Nayakshin S., 2012, MNRAS, 424, 666